Nanoscale
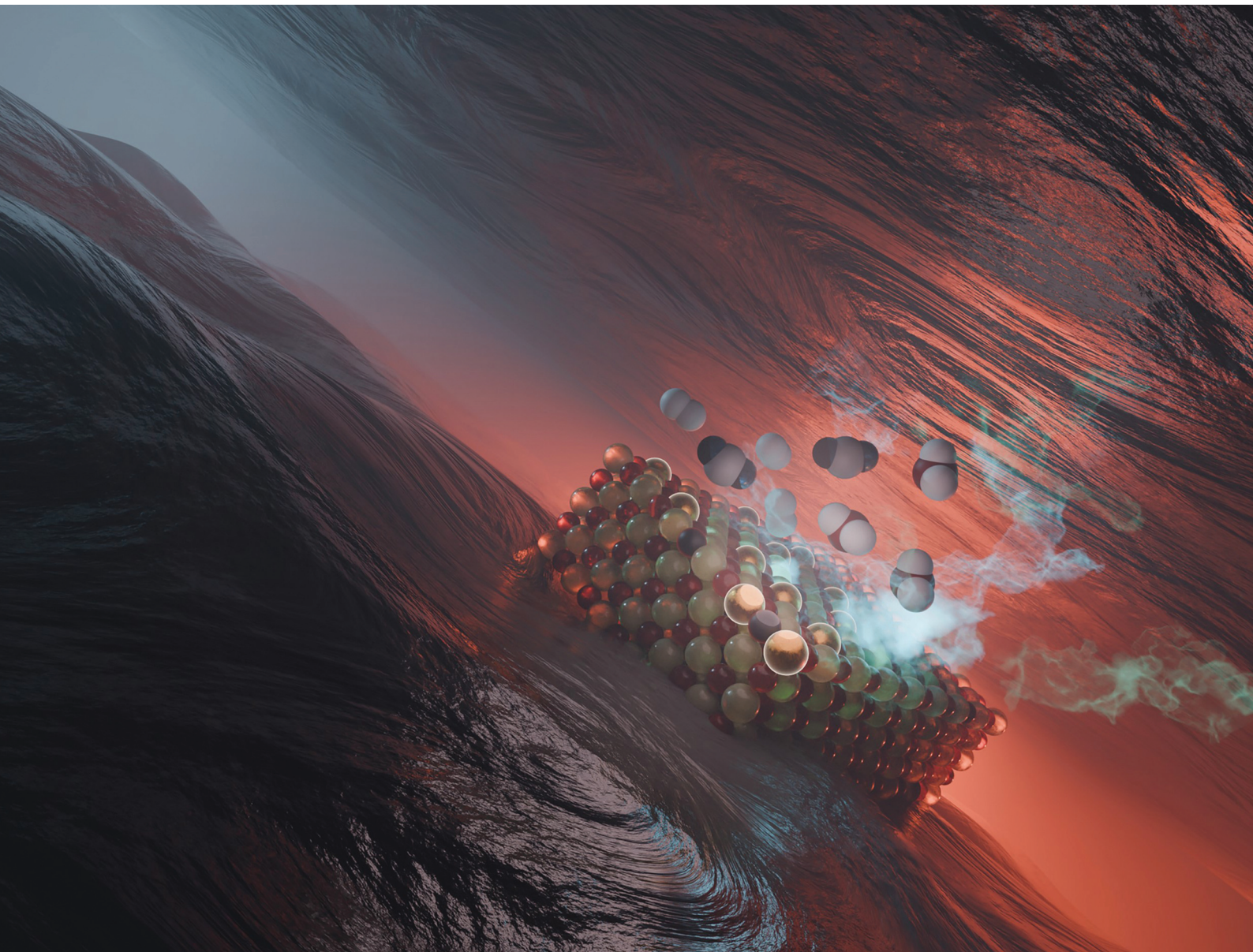
ROYAL SOCIETY
OF CHEMISTRY

COMMUNICATION
Anatoly I. Frenkel *et al.*
Unravelling the origin of reaction-driven aggregation and
fragmentation of atomically dispersed Pt catalyst on ceria
support

NCNST

COMMUNICATION

Check for updates

Unravelling the origin of reaction-driven aggregation and fragmentation of atomically dispersed Pt catalyst on ceria support†

Haodong Wang,[a] Hyuk Choi,[b] Ryuichi Shimogawa,[a,c] Yuanyuan Li,[d] Lihua Zhang,[e] Hyun You Kim [ID] [b] and Anatoly I. Frenkel [ID] *[a,f]

Metal–support interaction plays a crucial role in governing the stability and activity of atomically dispersed platinum catalysts on ceria support. The migration and aggregation of platinum atoms during the catalytic reaction leads to the redistribution of active sites. In this study, by utilizing a multimodal characterization scheme, we observed the aggregation of platinum atoms at high temperatures under reverse water gas shift reaction conditions and the subsequent fragmentation of platinum clusters, forming "single atoms" upon cooling. Theoretical simulations of both effects uncovered the roles of carbon monoxide binding on perimeter Pt sites in the clusters and hydrogen coverage in the aggregation and fragmentation mechanisms. This study highlights the complex effects of adsorbate and supports interactions with metal sites in Pt/ceria catalysts that govern their structural transformations under *in situ* conditions.

Introduction

"Single-atom" catalysts (SACs) have garnered significant attention for their enhanced activity and effective utilization of precious metals in different reactions.[1–7] Ceria stands out as a highly utilized support for stabilizing SACs, owing to its capacity to host single metal species and enhance the mobility of oxygen atoms for certain catalytic pathways.[8–11] However,

[a]Department of Materials Science and Chemical Engineering, Stony Brook University, Stony Brook, NY 11794, USA. E-mail: anatoly.frenkel@stonybrook.edu

[b]Department of Materials Science and Engineering, Chungnam National University, Daejeon 34134, Republic of Korea

[c]Mitsubishi Chemical Corporation, Science and Innovation Center, Yokohama 227-8502, Japan

[d]Chemical Sciences Division, Oak Ridge National Laboratory, Oak Ridge, TN 37831, USA

[e]Center for Functional Nanomaterials, Brookhaven National Laboratory, Upton, NY 11973, USA

[f]Division of Chemistry, Brookhaven National Laboratory, Upton, NY 11973, USA

the harsh reaction condtions, especially reducing conditions at elevated temperatures, can result in aggregation of single atoms. Extensive debates persist regarding whether "single atoms" or the nanoparticles are the active catalytic species in many reactions.[12–16] Therefore, it's crucial to explore the nature of the transformations between the "single atoms" and nanoparticles in reaction conditions and highlight the roles of metal–support and metal–adsorbate interactions in these transformations. In our previous work, we have shown the systematic evolution of platinum "single atoms" to form nanoparticles on ceria support under water gas shift reaction.[3] However, the unique roles of the gas adsorbates and metal–support interaction responsible for the aggretation of "single atoms" remain unknown.

In the current study, we focused on understanding how the realistic conditions of the reverse water gas shift (RWGS) reaction influence the interaction between Pt atoms and ceria support. To address this, we performed the temperature dependent studies of Pt nanoparticle catalysts upon cooling from their active state in RWGS conditions (at 300 °C) in two different atmospheres: (1) RWGS reaction mixture (CO_2 and H_2) and (2) CO. Combined *in situ* diffuse reflectance infrared Fourier transform spectroscopy (DRIFTS), *in situ* X-ray absorption spectroscopy (XAS) and *ex situ* high angle annular dark field – scanning transmission electron microscopy (HAADF-STEM) imaging were performed to reveal the distribution and local structure of Pt species on ceria support. The density functional theory (DFT) calculations were performed to provide insights into the roles of metal–adsorbates and metal–support interactions under reaction conditions at an atomic level.

Results and discussion

The Pt/CeO_2 catalyst, with a Pt weight loading of 0.94 wt%, was synthesized by using the wet impregnation method. The RWGS reaction was carried out at 300 °C under a gas mixture

of 5% CO_2 and 5% H_2 balanced in He with a total flow rate of 31.5 ml min^{-1}. The same sample was studied in RWGS conditions previously, alongside with the Pt/ceria-titania mixed support sample, and both samples were shown to undergo partial (for this sample) and nearly complete (for the Pt/ceria-titania sample) reduction to metal particles at 300 °C in RWGS conditions.[17] The as-prepared sample was determined to contain predominantly atomically dispersed Pt species on ceria support as reported previously.[18–20] HAADF-STEM imaging did not detect clusters or nanoparticles in the as-prepared sample (Fig. S1a†). DRIFTS results presented in Fig. 1 indicate that, under reaction conditions, the narrow peak at 2087 cm^{-1}, corresponding to the CO coordinated to the ionic Pt single site,[10,21] disappeared from the as-prepared sample after heating to 300 °C under reaction condition, indicating the Pt species aggregated into clusters or nanoparticles. The main contribution to the DRIFTS peak was at the 2064 cm^{-1}, which can be assigned to the well-coordinated sites (WC) of Pt clusters.[22,23] Surprisingly, after cooling down in different gas conditions, distinct structural transformations revealed *via* the changes in the CO coordination on the Pt clusters were observed. When cooling down under the RWGS reaction condition, a shoulder at 2010 cm^{-1} appeared which corresponds to the undercoodinated (UC) sites of the Pt clusters, as shown in Fig. 1(a).[24] The frequency and the peak intensity corresponding to the UC sites are known to change with CO coverage, environment of the Pt coordination site, and particle size.[22,23] In contrast, when cooling the sample down in CO flow conditions (5% CO balanced with He), a single narrow peak appeared at 2087 cm^{-1} (Fig. 1b), corresponding to the formation of ionic Pt single site, which indicated the fragmentation of Pt clusters. The lack of the 2010 cm^{-1} shoulder is an indication that the Pt atoms removed from the clusters were in the UC sites, *i.e.*, on and near the perimeter of the clusters.

It is intriguing to note that the same catalyst exhibited different structural evolutions after the reaction when cooling down and exposed to different gas conditions. We hypothesize that CO plays a pivotal role in the fragmentation of Pt clusters

during the cooling process. Due to the two different sources and thus roles of CO (as the RWGS product in the first experiment (Fig. 1a) and as a probe in the second experiment (Fig. 1(b)), we formulated the following questions guiding the work reported here. They are: (a) Can a stoichiometric amount of CO coordinated to the Pt induce the formation of Pt single sites? (b) Is the presence of excess amount of CO solely responsible for the observed changes? and (c) What are the fundamental mechanisms responsible for aggregation of Pt "single atoms" (SAs) and the subsequent fragmentation of Pt nanoparticles?

To decipher the factors leading to the fragmentation of Pt species, we conducted *in situ* X-ray absorption fine structure (XAFS) experiments which can provide detailed insights into the local environment of Pt species under reaction conditions. The Pt L_3 X-ray absorption near-edge structure (XANES) spectra are shown in Fig. 2(a). The spectrum for Pt/ceria is similar in intensity to, and shifted to the lower energies from the spectrum of α-PtO_2, consistent with previous work reporting the atomically dispersed nature of Pt/ceria sample.[17,19,20] The trends shown in Fig. 2(a) are consistent with those shown previously and indicate that the as-preapred sample contained predominantly atomically dispersed Pt species, while the Pt species partially aggregated under reaction condition at 300 °C.[17,18] After cooling the sample down to room temperature (RT) under reaction conditions, the white line intensity increased but remained lower than that in the spectra before reaction. In R space of the EXAFS spectra, as shown in Fig. 2(b), the relative ratio of Pt–Pt (second peak) to Pt–O (first peak) contributions decreases at RT in RWGS conditions. We conclude therefore that, averaging over the entire ensemble probed in the XAFS experiment, the coordination of Pt by O increased at room temperature compared to the results obtained at 300 °C. In order to resolve between different possible scenarios we performed fitting of Pt EXAFS spectra collected before and after the RWGS reaction.

A model incorporating Pt–O single scattering paths was employed to fit the room-temperature spectra of the as-prepared Pt/CeO_2 sample (Fig. S2a†) and the same sample after the end of the *in situ* RWGS reaction (Fig. S2b†). The best fit results are summarized in Table 1. The decrease of the Pt–O
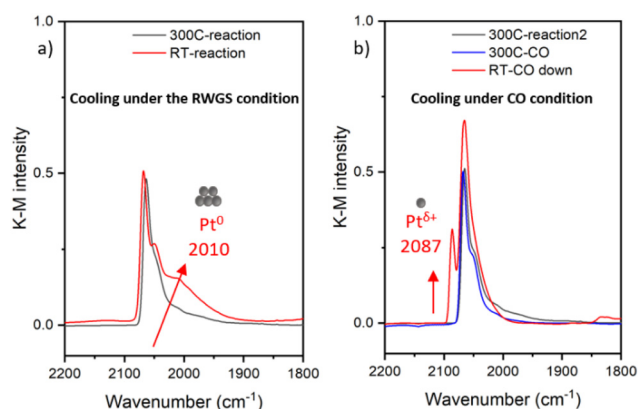

Fig. 1 DRIFTS results of Pt/CeO_2 catalysts under different gas conditions. (a) RWGS reaction at 300 °C and cooling down to RT; (b) RWGS reaction at 300 °C and change gas to CO then cooling down to RT.
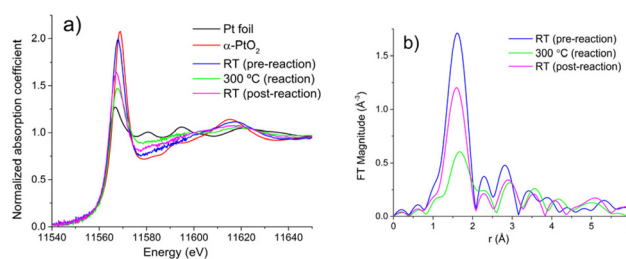

Fig. 2 Pt L_3 edge XAFS spectra of Pt/CeO_2 catalysts during the RWGS reaction shown in the XANES region, including the PtO_2 standard (a), and Fourier transform magnitude of the k^2-weighted EXAFS spectra using k-range from 2 to 10 $Å^{-1}$ (b).

Table 1 Summary of the EXAFS fitting results (the coordination number, bond length and mean square bond length disorder for the RT data shown in Fig. 2b (the results for the 300 °C were reported in ref. 17)). For all the fits, the k-range was: 2.5–13 Å^{-1}; the r-range: 1.0–2.2 Å. The S_0^2 value was obtained by first fitting Pt foil and then using the best fit result for (0.84) as a fixed parameter in the fits of all Pt spectra

Condition	Path	CN	R (Å)	σ^2 (Å^2)
Pre-RWGS	Pt–O	4.5(5)	2.00(1)	0.0015(11)
Post-RWGS	Pt–O	3.1(4)	2.00(1)	0.0014(13)

CN at 300 °C down to 1.7 ± 0.4 [17] compared to its pre-reaction value of *ca.* 4.5 (Table 1) implies that a significant fraction of Pt atoms that were initially dispersed on ceria has formed clusters in reaction conditions. The subsequent increase of the Pt–O CN up to *ca.* 3.1 (Table 1) in cooling down to RT in reaction conditions indicates that significant fraction of the clusters fragmented and formed atomically dispersed Pt. This observation corroborates the similar conclusion made on the basis of the DRIFTS results described above. We note that, although the presence of clusters and nanoparticles after the RWGS

reaction is evident in Fig. S1b,† the unambiguous detection of atomically dispersed Pt coexisting with the clusters was only possible by a correlated analysis of XAFS and DRIFTS presented above. In addition to the mechanisms proposed here, in principle, formation of partially oxidized shell in Pt nanoparticles may also explain the XANES and EXAFS data obtained while cooling the sample under reaction conditions, however, we ruled out that possibility due to the fact that the cooling was done under presence of hydrogen and in the absence of oxygen.

To explain the phenomena of the agglomeration and the fragmentation of the Pt in the RWGS reaction conditions and CO tituration conditions, we performed the DFT calculations using the model geometries of Pt species and CeO$_2$ support as described in Fig. S3.† The choice of the (100) facet for Pt sites was justified by us previously,[20] using a combination of multi-modal experimental results and DFT calculations for the Pt SAs on ceria prepared by the same method as in the present work. Firstly, the DFT-calculated binding energy, E_{bind}, of CO$_2$ (−0.39 eV) and H$_2$ (−2.27 eV) on Pt$_1$/CeO$_2$ and H$_2$ (0.19 eV) on CeO$_2$ indicates that the H$_2$ preferentially bind to Pt SAs initially
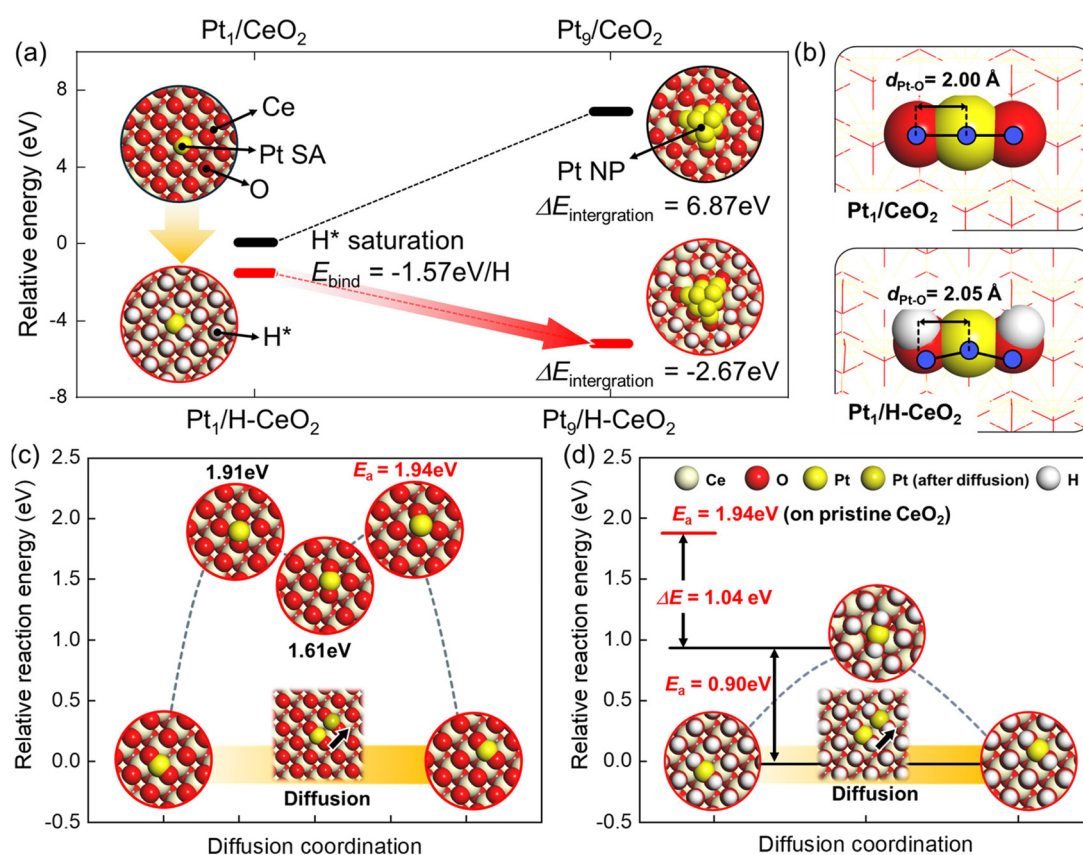

Fig. 3 The DFT-estimated energetics of the process of agglomeration of Pt atoms to Pt NPs on CeO$_2$ under the non-hydrogen (black lines) and RWGS (red lines) conditions (a). The Pt$_1$CeO$_2$ and Pt$_1$/H−CeO$_2$ indicate the DFT-constructed catalyst models under the non-hydrogen and RWGS conditions, respectively. (b) The Pt−O distances on the CeO$_2$ surface with and without H. (c and d) The diffusion kinetics and pathway of Pt SA on the CeO$_2$ and H-saturated CeO$_2$ surfaces. The black arrows indicate the diffusion direction of Pt SA along surfaces. The red-colored energy value is the activation barrier of diffusion.

(Fig. S4†). Interestingly, compared with the pristine CeO_2, H_2 can dissociatively bind to Pt SA. Because the H_2 dissociatively adsorbed on Pt and O of the CeO_2 surface spontaneously, the protons from gas-phased H_2 eventually saturate and cover the CeO_2 surface due to a low activation energy (E_a = 0.43 eV) of H diffusion along the CeO_2 (Fig. S5†). These results indicate that the Pt SA can act as the gateway for H_2 activation. Thus, we expect that the CeO_2 (100) surface is fully covered with protons under RWGS conditions.

Moreover, the saturation of H atoms on CeO_2 (100) results in intense stabilization of the Pt_1/CeO_2 (E_{bind} = −1.57 eV per H, presented in Fig. 3a). Based on the DFT-calculated results, we constructed the energetics for aggregation under non-hydrogen or RWGS conditions to compare the thermodynamic driving forces for aggregation of Pt SA to Pt NP (Fig. 3a). The $Pt_1/H–CeO_2$, which is H-saturated CeO_2 under RWGS conditions, exhibits the downhill energetics for integration of Pt NP, indicating that the Pt SA is likely to agglomerate. In contrast, because the formation of Pt NP under non-hydrogen conditions shows significant uphill energetics, the aggregation of Pt SA in Pt_1/CeO_2 is not thermodynamically feasible. Such thermodynamic results are explained by the difference in the cohesive energy of Pt NP and the interaction energy between Pt SA and oxide supports.

The bond length of Pt and O of the CeO_2 surface estimated by DFT calculation represents the interaction between the Pt SA and the CeO_2, which is presented in Fig. 3b. The atomic distance between Pt and O of the CeO_2 increases from 2.00 Å to 2.05 Å, which are at CeO_2 and H-saturated CeO_2, respectively. It indicates that the interaction between Pt and oxide support weakens under the RWGS condition due to the pre-covered protons on O of the CeO_2 surface. The interaction between Pt SA and oxide support results in the mobility of Pt SA along the CeO_2 surface. We further calculated the diffusion pathways of Pt SA on the CeO_2 (100) and H-saturated CeO_2 (100) surfaces to confirm the feasibility of kinetics for aggregation (Fig. 3c and d). The activation barrier for diffusion of Pt SA along the pristine CeO_2 (100) surface, E_a = 1.94 eV, is significantly higher than that along the H-saturated CeO_2 (100) (E_a = 0.90 eV). These results indicate that the RWGS conditions facilitate the integration of atomically dispersed Pt in the as-prepared sample into Pt clusters and nanoparticles due to reduced interaction between Pt and the CeO_2 support. We note that the EXAFS results for Pt–O bond lengths at RT (2.00 ± 0.01 Å) and 300 °C (2.00 ± 0.05 Å) are available[17] but the relatively large error bars at 300 °C make it impossible to verify these theoretical predictions.

In addition to the aggregation of atomically dispersed Pt species in RWGS conditions, the combined DRIFTS and XAFS results revealed also their subsequent partial fragmentation under CO condition. In order to identify the possible mechanisms of CO-induced fragmentation of Pt species, we performed DFT calculations to analyze two different effects required for the fragmentation of the perimeter Pt atoms: (A) the relatively weak interaction of perimeter Pt atoms in NPs and (B) the CO–CO repulsive interaction plus strong CO
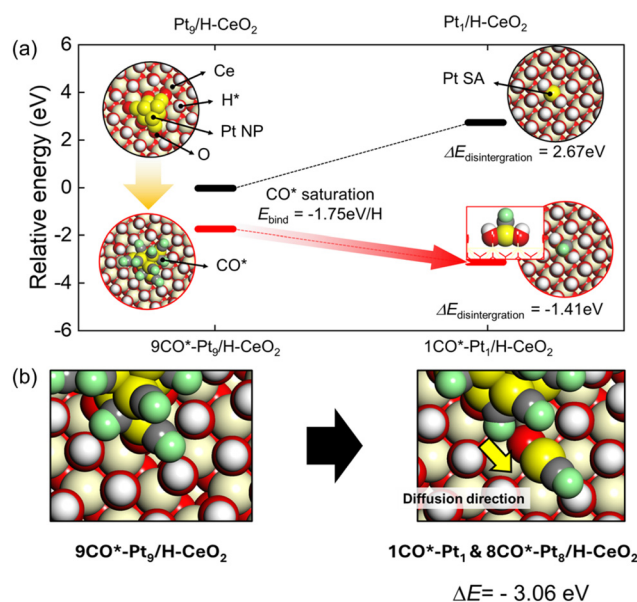

Fig. 4 The DFT-estimated fragmentations of Pt NP to Pt SA on Pt/CeO_2 under non-hydrogen and CO conditions. (a) The energetics for fragmentations of Pt NP are presented depending on conditions, which are non-hydrogen and CO conditions, denoting black and red-colored lines, respectively. (b) The thermodynamics of detachment of CO*–Pt from Pt NP. The yellow arrow indicates the diffusion direction of CO*–Pt SA.

binding to Pt forming Pt–CO complexes, which combine to facilitate the removal of Pt atoms. We established the energetics of fragmentation of Pt NP to Pt SAs depending on the treatment conditions, which are the non-hydrogen and CO conditions, to figure out the mechanism of fragmentation of Pt NPs (Fig. 4a). We hypothesized that, in an extreme case of low CO concentration, the Pt NP surface is relatively clean. In the second scenario, the CO saturates the Pt NP surface under the CO titration conditions. The formation energetics of Pt SA under non-hydrogen conditions is reversely estimated from the energy profile of integration of Pt NP under the RWGS corresponding to Fig. 3a. However, the $9CO*–Pt_9/$ $H–CeO_2$, which CO saturates, exhibits downhill energetics for the disintegration of Pt NP to Pt SA under the CO conditions. Thus, the fragmentation of Pt NP is derived from the CO*–Pt interaction, which results in the elongation of Pt–Pt atomic distance. Such an elongation of Pt–Pt distance is estimated from the DFT-constructed models (Fig. S6†). The average Pt–Pt distance extends from 2.61 Å to 2.72 Å, which are air and CO conditions, respectively. Such variation of distance change is approximately 5%, meaning that the Pt NP will be transformed into a disordered phase by loosening the bonding length of Pt–Pt due to the interaction of CO*–Pt. Furthermore, the detachment of CO*–Pt from Pt NP is significantly downhill, indicating that the CO-induced disintegration of Pt NP is thermodynamically favorable (Fig. 4b). Thus, we suggest that the interaction between CO and Pt influenced the phase of Pt NP, which is eventually interspersed as Pt SA and Pt NP.

Conclusions

By employing combined DRIFTS and XAFS study, we proved the aggregation of atomically dispersed Pt species under the RWGS reaction and the following fragmentation of Pt nanoparticles to Pt single atoms under CO condition. DFT calculations revealed that the interaction strength between Pt and CeO_2 is compromised by Pt–OH* bonding on H-covered CeO_2. Furthermore, the elongation of Pt–Pt distance, induced by Pt–CO* bonding, contributes to the detachment of Pt–CO* units from Pt clusters. Combined use of theory and multimodal, *in situ*, experimental results led to the understanding of the aggregation and fragmentation details that we posed in the beginning. While we conclusively attribute the observed (by DRIFTS) fragmentation under CO titration conditions to the strong Pt–CO interaction, we can also infer, from the appearance of the UC sites under RWGS conditions at RT, that even under stoichiometric conditions, the tendency to fragmentation exists. Further work will be aimed at systematically understanding the dependence of aggregation and fragmentation trends on the composition of the support and the adsorbate flow conditions.

Author contributions

H. W., Y. L. and A. I. F. proposed the project and designed the experiments. R. S. collected *in situ* XAFS data with remote support from H. W. and A. I. F. H. W. prepared the catalysts and analyzed XAFS data under A. I. F. supervision. H. W. and R. S. performed *in situ* DRIFTS measurements. H. C. and H. Y. K. conducted DFT calculations. L. Z. conducted HAADF-STEM characterization. H. W., H. C. and A. I. F. wrote the manuscript with contributions from all authors.

Conflicts of interest

There are no conflicts to declare.

Acknowledgements

References

1 L. X. Chen, S. I. Allec, M. T. Nguyen, L. Kovarik, A. S. Hoffman, J. Y. Hong, D. Meira, H. H. Shi, S. R. Bare, V. A. Glezakou, R. Rousseau and J. Szanyi, *J. Am. Chem. Soc.*, 2023, **145**, 10847–10860.

2 X. Li, X. I. Pereira-Hernandez, Y. Z. Chen, J. Xu, J. K. Zhao, C. W. Pao, C. Y. Fang, J. Zeng, Y. Wang, B. C. Gates and J. Y. Liu, *Nature*, 2022, **611**, 284–288.

3 Y. Y. Li, M. Kottwitz, J. L. Vincent, M. J. Enright, Z. Y. Liu, L. H. Zhang, J. H. Huang, S. D. Senanayake, W. C. D. Yang, P. A. Crozier, R. G. Nuzzo and A. I. Frenkel, *Nat. Commun.*, 2021, **12**, 914.

4 L. C. Li, S. Miyazaki, S. Yasumura, K. W. Ting, T. Toyao, Z. Maeno and K. I. Shimizu, *ACS Catal.*, 2022, **12**, 2639–2650.

5 X. D. Chen, X. Su, B. L. Liang, X. L. Yang, X. Y. Ren, H. M. Duan, Y. Q. Huang and T. Zhang, *J. Energy Chem.*, 2016, **25**, 1051–1057.

6 L. Nguyen, S. Zhang, L. Wang, Y. Li, H. Yoshida, A. Patlolla, S. Takeda, A. I. Frenkel and F. Tao, *ACS Catal.*, 2016, **6**, 840–850.

7 S. Zhang, Y. Tang, L. Nguyen, Y.-F. Zhao, Z. Wu, T.-W. Goh, J. J. Liu, Y. Li, T. Zhu, W. Huang, A. I. Frenkel, J. Li and F. F. Tao, *ACS Catal.*, 2018, **8**, 110–121.

8 D. Jiang, G. Wan, C. E. García-Vargas, L. Z. Li, X. I. Pereira-Hernández, C. M. Wang and Y. Wang, *ACS Catal.*, 2020, **10**, 11356–11364.

9 A. Jan, J. Shin, J. Ahn, S. Yang, K. J. Yoon, J. W. Son, H. Kim, J. H. Lee and H. I. Ji, *RSC Adv.*, 2019, **9**, 27002–27012.

10 L. Nie, D. H. Mei, H. F. Xiong, B. Peng, Z. B. Ren, X. I. P. Hernandez, A. DeLariva, M. Wang, M. H. Engelhard, L. Kovarik, A. K. Datye and Y. Wang, *Science*, 2017, **358**, 1419–1423.

11 F. Zhang, Z. Liu, S. Zhang, N. Akter, R. M. Palomino, D. Vovchok, I. Orozco, D. Salazar, J. A. Rodriguez, J. Llorca, J. Lee, D. Kim, W. Xu, A. I. Frenkel, Y. Li, T. Kim and S. D. Senanayake, *ACS Catal.*, 2018, **8**, 3550–3560.

12 E. Fernández, L. C. Liu, M. Boronat, R. Arenal, P. Concepcion and A. Corma, *ACS Catal.*, 2019, **9**, 11530–11541.

13 F. Wang, Z. Li, H. H. Wang, M. Chen, C. B. Zhang, P. Ning and H. He, *Nano Res.*, 2022, **15**, 452–456.

14 J. Jones, H. F. Xiong, A. T. Delariva, E. J. Peterson, H. Pham, S. R. Challa, G. S. Qi, S. Oh, M. H. Wiebenga, X. I. P. Hernández, Y. Wang and A. K. Datye, *Science*, 2016, **353**, 150–154.

15 I. E. L. Stephens, J. S. Elias and Y. Shao-Horn, *Science*, 2015, **350**, 164–165.

16 B. T. Qiao, A. Q. Wang, X. F. Yang, L. F. Allard, Z. Jiang, Y. T. Cui, J. Y. Liu, J. Li and T. Zhang, *Nat. Chem.*, 2011, **3**, 634–641.

17 H. Wang, R. Shimogawa, L. Zhang, L. Ma, S. N. Ehrlich, N. Marinkovic, Y. Li and A. I. Frenkel, *Commun. Chem.*, 2023, **6**, 264.

18 H. Wang, M. Kottwitz, N. Rui, S. D. Senanayake, N. Marinkovic, Y. Li, R. G. Nuzzo and A. I. Frenkel, *ACS Appl. Mater. Interfaces*, 2021, **13**, 52736–52742.

19 H. D. Wang, N. Rui, S. D. Senanayake, L. H. Zhang, Y. Y. Li and A. I. Frenkel, *J. Phys. Chem. C*, 2022, **126**, 16187–16193.

20 M. Kottwitz, Y. Y. Li, R. M. Palomino, Z. Y. Liu, G. J. Wang, Q. Wu, J. H. Huang, J. Timoshenko, S. D. Senanayake, M. Balasubramanian, D. Y. Lu, R. G. Nuzzo and A. I. Frenkel, *ACS Catal.*, 2019, **9**, 8738–8748.

21 L. DeRita, S. Dai, K. Lopez-Zepeda, N. Pham, G. W. Graham, X. Q. Pan and P. Christopher, *J. Am. Chem. Soc.*, 2017, **139**, 14150–14165.

22 M. J. Kale and P. Christopher, *ACS Catal.*, 2016, **6**, 5599–5609.

23 T.-S. Kim, C. R. O'Connor and C. Reece, *Nat. Commun.*, 2024, **15**, 2074.

24 P. F. Xie, T. C. Pu, A. M. Nie, S. Hwang, S. C. Purdy, W. J. Yu, D. Su, J. T. Miller and C. Wang, *ACS Catal.*, 2018, **8**, 4044–4048.